Matter

Article

Operando leaching of pre-incorporated Al and mechanism in transition-metal hybrids on carbon substrates for enhanced charge storage

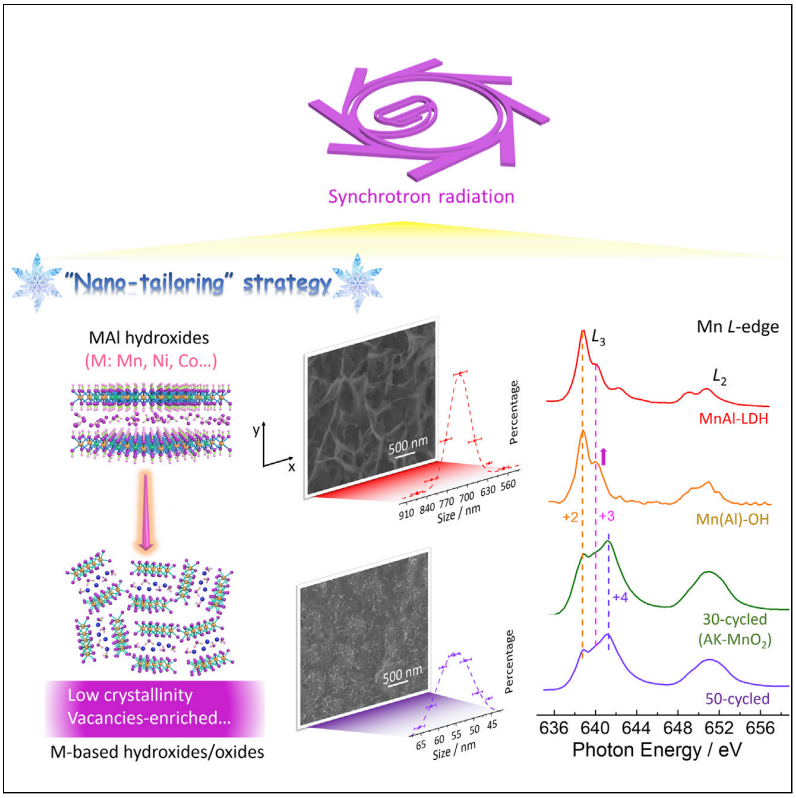

With M^{2+}Al hydroxides as the precursor, a universal "nano-tailoring" process is developed to configure low-crystallinity, defective materials with enriched edge-active sites for boosting the charge-storage capability. Soft XAS and Raman mapping techniques are adopted to finely track the dynamic reconstruction principles and intrinsic active sites. And it is found that the reducibility of M^{2+} serves as the key descriptor for the reconstruction rate.

Understanding
Dependency and conditional studies on material behavior

Wei Guo, Feipeng Yang, Chang Yu, ..., Qiuyu Zhang, Jinghua Guo, Jieshan Qiu

chang.yu@dlut.edu.cn (C.Y.)
qyzhang@nwpu.edu.cn (Q.Z.)
jguo@lbl.gov (J.G.)
jqiu@dlut.edu.cn (J.Q.)

Highlights

A "nano-tailoring" strategy via electrochemical leaching of Al species is proposed

Defective and highly active materials were formed via the "nano-tailoring" strategy

The integrated oxygen vacancies can boost charge storage of potassium-birnessite

The reducibility of M^{2+} is identified as the key descriptor for the reconstruction rate

Guo et al., Matter 4, 1–17
September 1, 2021
https://doi.org/10.1016/j.matt.2021.06.035

Please cite this article in press as: Guo et al., *Operando* leaching of pre-incorporated Al and mechanism in transition-metal hybrids on carbon substrates for enhanced charge storage, Matter (2021), https://doi.org/10.1016/j.matt.2021.06.035

Matter

CellPress

Article

Operando leaching of pre-incorporated Al and mechanism in transition-metal hybrids on carbon substrates for enhanced charge storage

Wei Guo,[1,2,3] Feipeng Yang,[2] Chang Yu,[1,*] Yuanyang Xie,[1] Jiuke Chen,[4] Yisheng Liu,[2] Yang Zhao,[2] Juan Yang,[6] Xuefei Feng,[2] Shaofeng Li,[1] Zhao Wang,[1] Jinhe Yu,[1] Kunlun Liu,[1] Kun Qian,[4] Mesfin Tsige,[4] Qiuyu Zhang,[3,*] Jinghua Guo,[2,*] and Jieshan Qiu[1,5,7,*]

SUMMARY

Insufficient exposure and utilization of active sites often induces an inferior reactivity for transition-metal-based two-dimensional (2D) materials. In response, we for the first time propose a universal "nano-tailoring" strategy to incorporate abundant defects and active sites into low-crystallinity nanosheets by electrochemically leaching of Al species. With MnAl layered double hydroxides (LDHs) as a representative example, potassium-birnessite MnO_2 (AK-MnO_2) with oxygen vacancies and abundant edge sites is successfully produced. The oxygen vacancies are shown to help optimize the electron-transfer and ion-adsorption capability. These integrated advantages endow the AK-MnO_2 with a high capacitance value of 239 F g^{-1} at 100 A g^{-1}. By further combining with soft X-ray absorption spectroscopy techniques, we unravel that the reducibility of M^{2+} in M^{2+}Al-LDH serves as the key descriptor for the reconstruction rate. This "nano-tailoring" strategy can provide some important implications and clues to manipulating 2D materials for efficient energy storage and conversion.

INTRODUCTION

With the development of social science and technology, a strong need for fast, sustainable, and high-power energy-storage systems has led to the quick development of supercapacitors, which can be divided into two kinds: electric double-layer capacitors (EDLCs) and pseudocapacitors (PCs).[1,2] Compared with EDLCs, the PCs are generally endowed with reversible surface/near-surface reactions to store more charges, thus demonstrating highly enhanced capacitive performance.[3–5] For configuring better PCs, rational modulation and optimization of reactive sites to activate the intrinsic properties of electrode materials are highly desired, serving as the key point for advancing energy storage.[6–8]

Generally, transition-metal materials with intrinsic/extrinsic pseudocapacitive properties are identified as being highly effective and indispensable for electrochemical energy storage because of their high theoretical capacitance, superior flexibility, and excellent electronic properties.[9–11] Nevertheless, the inferior actual performance, which is far lower than the theoretical value, is the main barrier to the practical applications.[12–14] This is mainly caused by poor accessibility of active sites and largely restricted reaction dynamics. To solve these issues, developing new and effective physical or chemical methods to ameliorate the intrinsic redox reaction

Progress and potential

From the viewpoint of optimizing charge-storage dynamics, we for the first time propose a universal "nano-tailoring" strategy to fabricate low-crystalline and highly active materials via electrochemically dynamic leaching of pre-incorporated Al. With M^{2+}Al hydroxides as the precursor, potassium-birnessite MnO_2 with abundant defective sites and enriched edge-active sites is configured, resulting in the enhanced charge-storage capability. Soft XAS and Raman mapping techniques are adopted to finely track the dynamic reconstruction principles and intrinsic active sites. It is found that the reducibility of M^{2+} serves as the key descriptor for the reconstruction rate, which correspondingly is divided into two branches: oxidization-boosting type and non-oxidization type. This work can provide a novel avenue and spark new ideas to electrochemically modulate and ameliorate electrode materials for advanced energy storage and conversion applications in the future.

Please cite this article in press as: Guo et al., *Operando* leaching of pre-incorporated Al and mechanism in transition-metal hybrids on carbon substrates for enhanced charge storage, Matter (2021), https://doi.org/10.1016/j.matt.2021.06.035

characteristics and the surface microstructure properties simultaneously is highly desired.

It is widely accepted that high-crystallinity materials generally suffer from difficulties in expansion and extraction of lattice planes, thus leading to hindered permeation and transport of electrolyte ions to some degree.[15] In addition, the highly ordered structure would be dynamically unfavorable for the sufficient reaction of redox species. In this regard, regulating the crystallinity of these types of materials may lead to the positive modulation of redox reaction dynamics. In extreme cases, it has been identified that transforming the crystalline structure into a low-crystallinity/amorphous one can introduce many internal disorders, grain boundaries, and dangling bonds, leading to an effective exposure of active sites, facilitated ion transport, and promoted reactivity.[16,17] In addition, the *in situ* introduced defects can produce many coordinately unsaturated and accessible sites, further enlarging the active area for optimization of the redox dynamics.[18–21] These defects can also somehow modulate the electronic structure and surface chemistry, thereby promoting interfacial electronic transfer and mass transport.[22–25] With this information in mind, it is easy to believe and anticipate that a much hastened charge-storage process can be realized accordingly. For example, a previous result demonstrated that amorphous $Ni(OH)_2$ delivered a capacity about 20% and 60% higher than that of the crystalline α- and β-$Ni(OH)_2$, respectively.[26] Low-crystallinity FeOOH, derived from the crystalline α-Fe_2O_3, can demonstrate an exceptionally high capacitance value of 1,066 F g^{-1}, superior to that of most Fe-based electrode materials.[27] Another tough issue for configuration is the formation of a bulky structure in some cases, which leads to a fairly long electron-transfer path and relatively sluggish ion diffusion. Accordingly, many endeavors have been made to endow tailor-made electrode materials with more surface and edge active sites, leading to an optimization of both capacitance and rate performance.[28–30] To sum up, holistic activation in terms of both crystalline engineering and nanostructure is desperately warranted for the promotion of electrochemical performance.

Electrochemical configuration/modulation techniques feature sound tunability toward the electronic structure, phase components, and defective sites, attracting great attention in recent years in energy-related fields.[31–33] Moreover, the low energy cost and time-saving characteristics give it great potential for large-scale applications. It has been proved that *in situ* leaching of inactive species in the electrochemical environment and the corresponding phase regulation can help produce a low-crystallinity and defect-enriched microstructure with tuned morphologies.[34,35] In this regard, further progress requires the development of a universal methodology/strategy to tailor the generally adopted materials into highly active ones with modulated structures in terms of nano/micro and atomic scales. To the best of our knowledge, aluminum, as a typical amphoteric metal element, displays a tendency to spontaneously dissolve in alkaline electrolytes, while this is thermodynamically unfavorable for transition-metal elements. In addition, Al-based transition-metal hybrids have a big family, including double/triple/multiple oxides, hydroxides, sulfides, and so on. Accordingly, it is expected that pre-incorporating Al into the lattice of transition-metal hybrids, followed by its *in situ* leaching, can generate a series of advanced materials with promoted reactivity, which remain less concerning and require more attention and detailed explorations.

Herein, a universal "nano-tailoring" strategy, via the *operando* leaching of pre-incorporated Al driven by electrochemical effects, is first proposed for realizing the holistic activation of transition-metal hybrids. Using MnAl layered double

[1]State Key Lab of Fine Chemicals, School of Chemical Engineering, Liaoning Key Lab for Energy Materials and Chemical Engineering, Dalian University of Technology, Dalian 116024, China

[2]Advanced Light Source (ALS), Lawrence Berkeley National Laboratory, Berkeley, CA 94720, USA

[3]School of Chemistry and Chemical Engineering, Northwestern Polytechnical University, Xi'an 710129, PR China

[4]Department of Polymer Science, The University of Akron, Akron, OH 44325, USA

[5]College of Chemical Engineering, Beijing University of Chemical Technology, Beijing 100029, China

[6]School of Chemical Engineering and Technology, Xi'an Jiaotong University, Xi'an 710049, China

[7]Lead contact

*Correspondence: chang.yu@dlut.edu.cn (C.Y.), qyzhang@nwpu.edu.cn (Q.Z.), jguo@lbl.gov (J.G.), jqiu@dlut.edu.cn (J.Q.)

https://doi.org/10.1016/j.matt.2021.06.035

Please cite this article in press as: Guo et al., *Operando* leaching of pre-incorporated Al and mechanism in transition-metal hybrids on carbon substrates for enhanced charge storage, Matter (2021), https://doi.org/10.1016/j.matt.2021.06.035

hydroxides (LDHs) as a demonstration, we show that low-crystallinity potassium-birnessite MnO_2 (AK-MnO_2) can be produced quickly after the "nano-tailoring" process. With the help of soft X-ray absorption spectroscopy (sXAS), the structural evolution is finely tracked and decoupled. Interestingly, due to the irreversible leaching of Al and the intercalation of K^+, the microstructure may undergo the emergence and release of internal strain, resulting in a positively tailored microstructure with enriched edge sites and oxygen vacancies. Also, density functional theory (DFT) calculation demonstrates that the introduced oxygen vacancies would be capable of promoting charge transfer and facilitating the adsorption of electrolyte ions, leading to optimized reaction kinetics for charge storage. As such, the as-formed AK-MnO_2 hybrids can deliver a high capacitance value of 356 F g^{-1} at 1 A g^{-1}, with a high retention rate of up to 67% at a super-large current density of 100 A g^{-1}, indicative of a superior rate performance. More importantly, the universality of the "nano-tailoring" process to generate low-crystallinity nanosheets with enriched active sites is deeply verified and decoupled. We reveal that the leaching transformation is highly dependent on the reducibility of the adopted M^{2+}, which acts as a prominent factor for the reconstruction rate. It is believed that the unique and universal "nano-tailoring" strategy can stimulate broad interest and inspiration of researchers to configure novel and highly efficient materials with positively tuned properties.

RESULTS AND DISCUSSION

Nano tailoring of LDH precursors and the tracking of dynamic microstructure

As illustrated in Figure 1A, the "nano-tailoring" strategy involves M^{2+}Al-based binary hydroxides as the precursor, where the molecular breakage and reconstruction happens during the electrochemical scanning process in an alkaline medium. As a typical example, during the "nano-tailoring" process, the MnAl-LDH will undergo a transformation into MnAl-based hydroxides, accompanied by partial leaching of Al, when soaked in an alkaline electrolyte for a short time (2 min), yielding Mn(Al)-OH as the intermediate. Subsequently, it will be reconstructed into low-crystallinity birnessite-type MnO_2 with K^+ in the interlayer after cyclic voltammetry (CV) cycling treatment, denoted as AK-MnO_2. The dynamic reconstruction is *ex situ* tracked by scanning electron microscopy (SEM) images and the corresponding size distributions. As shown in Figures 1B–1D, the large LDH nanosheets are broken and reconstructed to much smaller ones with a higher stacking density. The average size decreases from 726 nm for the MnAl-LDH to 202 nm for the Mn(Al)-OH hybrids, and finally to 55 nm for the AK-MnO_2 hybrids (about 13 times decrease in size). Notably, the small and dense nanosheets would deliver more abundant active sites and feature numerous short-distance channels for fast charge transfer, and thus are beneficial for highly efficient charge storage.

The microstructure is further uncovered by transmission electron microscopy (TEM) images. As depicted in Figure S1A, the MnAl-LDH precursor displays a large size, and a lattice spacing of 0.26 nm corresponds to the (012) plane of LDH. For the Mn(Al)-OH, a broken structure with numerous *in situ*-formed holes can be observed, and the lattice spacing of 0.33 nm corresponds to the (100) plane of $Mn(OH)_2$ (Figure S1B). Impressively, the well-tailored AK-MnO_2 with densely stacked and ultrasmall nanosheet microstructure (Figure 1E) displays a low crystallinity, as shown in the high-resolution (HR)-TEM image (Figure 1F). It is further identified by the result of selected area electron diffraction (SAED), where no lattice patterns can be detected (Figure 1F), indicative of the generation of lattice distortion and randomly stacked internal construction. Furthermore, as presented by high-angle annular dark-field scanning TEM (HAADF-STEM) images and the corresponding elemental

Please cite this article in press as: Guo et al., *Operando* leaching of pre-incorporated Al and mechanism in transition-metal hybrids on carbon substrates for enhanced charge storage, Matter (2021), https://doi.org/10.1016/j.matt.2021.06.035

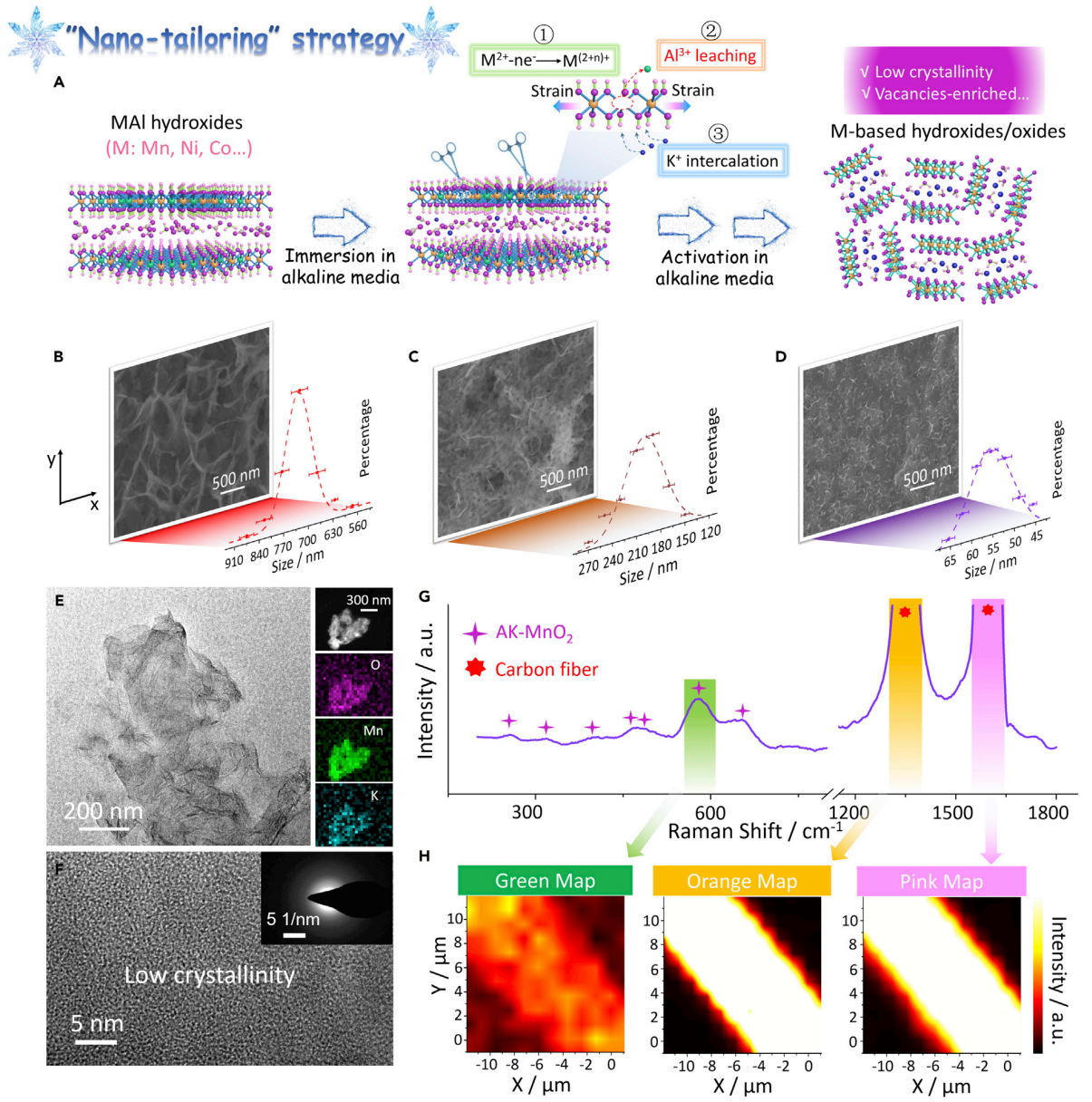

Figure 1. A brief introduction to nano tailoring and its application for configuring the low-crystallinity AK-MnO_2 hybrids

(A) Schematic illustration of the "nano-tailoring" strategy for the formation of low-crystallinity hydroxides/oxides. Purple, pink, orange, green, blue, and gray balls correspond to O, H, Mn (Co, Ni, ...), Al, K, and N atoms, respectively.

(B–D) SEM images and corresponding size distribution of the (B) MnAl-LDH, (C) Mn(Al)-OH, and (D) AK-MnO_2 nanosheets.

(E) TEM image and the corresponding elemental mapping images of the AK-MnO_2 nanosheets.

(F) HR-TEM image of the AK-MnO_2 nanosheets and the corresponding SAED pattern.

(G and H) Raman spectrum (G) and the corresponding mapping images (H) of the AK-MnO_2 hybrids.

Please cite this article in press as: Guo et al., *Operando* leaching of pre-incorporated Al and mechanism in transition-metal hybrids on carbon substrates for enhanced charge storage, Matter (2021), https://doi.org/10.1016/j.matt.2021.06.035

maps, the Mn, O, and K elements are uniformly distributed on the surface of the AK-MnO_2 (Figure 1E). Also, we carried out atomic force microscopy (AFM) characterization to better study the morphology of the AK-MnO_2. In Figure S2, the ultrathin and wrinkled nanosheet morphology with a thickness of about 7.7 nm is presented. In addition, the AK-MnO_2 demonstrates a highly increased surface area (157 $m^2\ g^{-1}$) as well as more abundant pore structure (Figure S3), compared with the MnAl-LDH (58 $m^2\ g^{-1}$). The enlarged surface area, enabled by the novel "nano-tailoring" process, can help give access to more electrolyte ions at a given time and shorten the transport distance, thus accounting for the enhanced charge storage.

The "nano-tailoring" process of the MnAl-LDH is further decoupled by X-ray diffraction (XRD) patterns (Figure S4). Notably, the intense peaks located at 26.4°, 43.1°, 54.6°, and 77.6° can be indexed to the characteristic peaks of carbon paper (CP). For the MnAl-LDH hybrids, the peaks at 10.1°, 20.2°, 33.1°, 36.4°, and 58.8° can be indexed to the (003), (006), (012), (015), and (110) planes of the LDH phase, respectively. Explicitly, for the Mn(Al)-OH hybrids, the peaks at 18.8°, 31.6°, 36.8°, 49.9°, and 59.5° can be indexed to the (001), (100), (101), (102), and (111) diffraction planes of $Mn(OH)_2$ (JCPDS card no. 18-0787), respectively, indicative of the phase transformation from the MnAl-LDH to the Al-doped $Mn(OH)_2$ phase. However, as for the AK-MnO_2, it displays only one significant peak at about 12.7°, as well as an indiscernible wide band in the range of 35° to 40°. This implies the low-crystallinity/amorphous features of the [MnO_6] octahedra laminate.[36,37] Notably, an increase of interlayer spacing from Mn(Al)-OH (d spacing: 4.7 Å) to AK-MnO_2 (d spacing: 7.0 Å) can be attributed to a certain amount of K^+ intercalated into the interlayer. To further confirm the existing species, Raman measurements were carried out. For the AK-MnO_2 hybrids, the characteristic peaks at 265, 317, 396, 469, 578, and 654 cm^{-1} are matched with those of birnessite-type MnO_2 with a little shift (Figure 1G), attributed to the varied ion radius between K^+ and Na^+.[38] And the intense peaks at 1,350 and 1,580 cm^{-1} could be indexed to the D and G bands of CP. Moreover, Raman maps were recorded in the green, orange, and pink regions (as marked in Figure 1G), where the uniform distribution for the signals of the CP (orange and pink) and the AK-MnO_2 (green) are presented in the maps (Figure 1H), indicative of the intimate interaction between them.

sXAS and theoretical calculation decoupling of the fine structure

The sXAS technique was used to decouple the fine structure of the as-formed hybrids and understand the dynamic phase reconstruction process. The mechanism of sXAS is illustrated in Figure 2A (refer to Yang and Devereaux and Lin et al.).[39,40] To be specific, the incident X-ray can induce the transition of electrons to the excited state and produce a core hole *in situ*. Then the decay of the excited-state electrons to the same core hole generates elastic energy to be detected.[39] sXAS is available to probe the chemical conditions of materials from surface to bulk. And the generated signals can be divided into total electron yield (TEY; depth: 2–5 nm) and total fluorescence yield (TFY; depth: about 50 nm).[41] The Mn *L*-edge soft XAS spectra are shown in Figure 2B. It is worth noting that the typical peaks at 638.8, 640.2, and 641.6 eV can be assigned to Mn^{2+}, Mn^{3+}, and Mn^{4+}, respectively, while the peak intensity is generally used to identify the relative content.[42] Clearly, for the MnAl-LDH, the peak at 638.8 eV is much more intensive than the others, implying that the Mn primarily exists in the +2 status. Compared with the MnAl-LDH, the Mn(Al)-OH hybrids are also dominated by Mn^{2+}, despite the slight increase in peak intensity of Mn^{3+}. Interestingly, the Mn^{4+} ions are dominant for the as-formed AK-MnO_2, where a certain amount of Mn^{3+} remained. It is noteworthy that the charge compensation can be realized by the intercalation of K^+, which is described below in detail.

Please cite this article in press as: Guo et al., *Operando* leaching of pre-incorporated Al and mechanism in transition-metal hybrids on carbon substrates for enhanced charge storage, Matter (2021), https://doi.org/10.1016/j.matt.2021.06.035

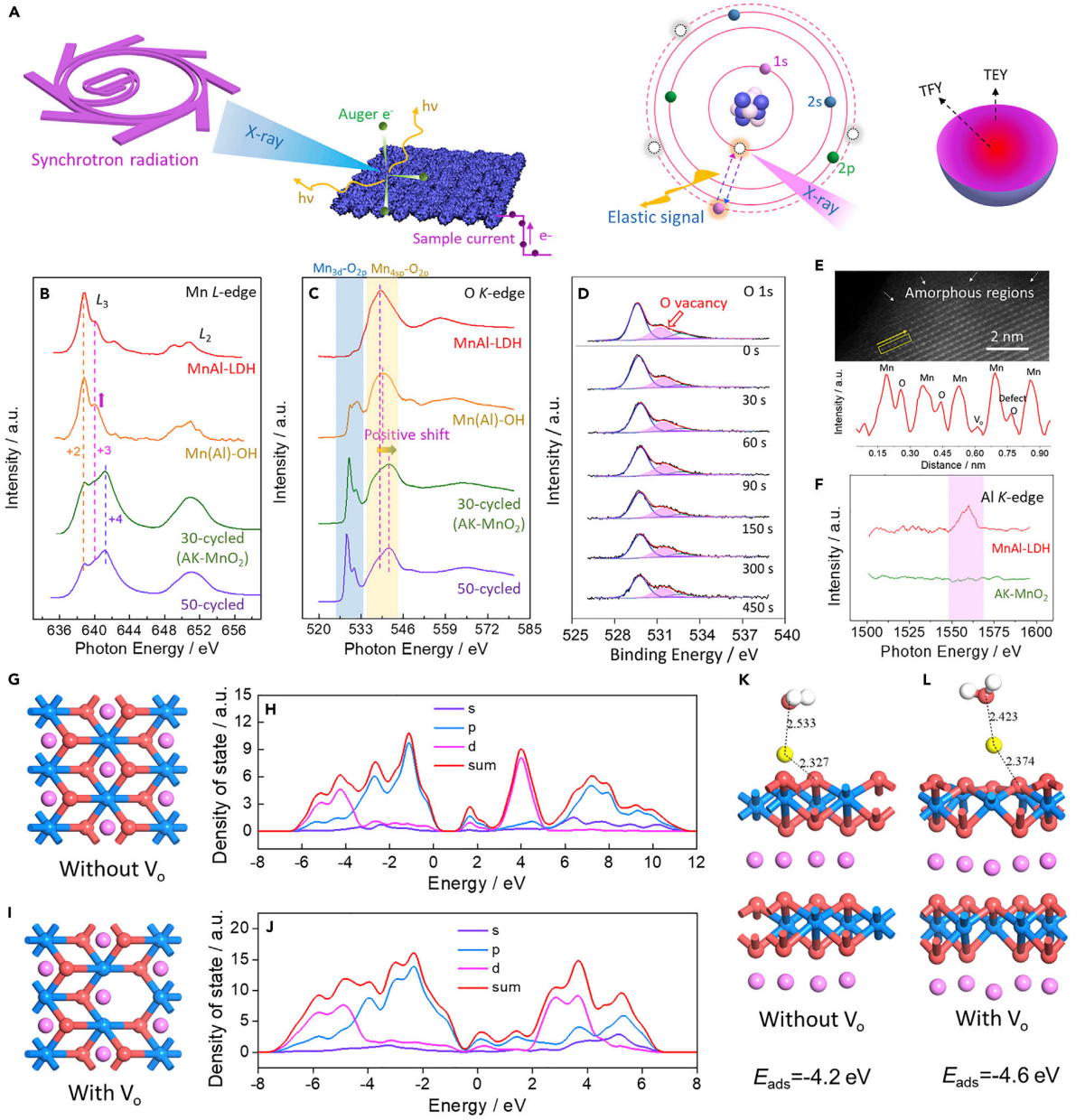

Figure 2. Fine-structure characterization and theoretical calculation analysis

(A) Schematic illustration of sXAS mechanism and its two types of mode with different probe depths.

(B and C) TEY scans: Mn *L*-edge (B) and O *K*-edge (C) of the MnAl-LDH, Mn(Al)-OH, and 30-cycled (AK-MnO_2) and 50-cycled hybrids.

(D) O 1s spectra of the AK-MnO_2 hybrids.

(E) HAADF-STEM image of the AK-MnO_2, and the intensity profile along the selected rectangular regions, which suggests the missed/defective O atoms on the surface.

(F) TFY scan for Al *K*-edge of the MnAl-LDH and AK-MnO_2 hybrids.

(G and H) Molecular structure of the pure AK-MnO_2 (G) and the corresponding density of state (DOS) curves (H).

(I and J) Molecular structure of the AK-MnO_2 with oxygen vacancies (V_o; I) and the corresponding DOS curves (J).

(K and L) Schematic adsorption models for hydrated sodium ion on the surface of the AK-MnO_2 without (K) and with (L) oxygen vacancies.

Please cite this article in press as: Guo et al., *Operando* leaching of pre-incorporated Al and mechanism in transition-metal hybrids on carbon substrates for enhanced charge storage, Matter (2021), https://doi.org/10.1016/j.matt.2021.06.035

Moreover, compared with the 30-cycled sample (AK-MnO_2), no further obvious changes in Mn *L*-edge are found after 50 cycles, implying that a stable status can be attained after 30 cycles. These results correspond finely to the Mn 2p and Mn 3s X-ray photoelectron spectroscopy (XPS) results (Figure S5). To gain a more complete picture of the reconstruction process, the O *K*-edge characterization was conducted (Figure 2C). The pre-edge region (below 533 eV) and broad-band region (over 533 eV) can be attributed to the transition of O 1s to Mn 3d and O 2p hybrid-state orbital, and O 1s to Mn 4sp and O 2p hybrid-state orbital, respectively. Generally speaking, the positive shift of the broad band can indicate an increase in Mn valence.[43] Compared with the MnAl-LDH, there is no detectable shift of the broad band for the Mn(Al)-OH, indicative of the unobvious oxidation of Mn species. Nevertheless, the significantly positive shift can be detected for the 30-cycled sample (AK-MnO_2), indicative of the oxidation of Mn species to a great degree. The 50-cycled sample demonstrates no more shift compared with the AK-MnO_2, indicative of complete transformation after 30 electrochemical cycles, very consistent with the results we mentioned above.

For the C *K*-edge spectra (Figure S6), the two new peaks at 299 and 302 eV, which correspond to the characteristic peaks of K L_3- and L_2-edge,[44] emerge for 30- and 50-cycled electrodes, indicative of the intercalation of K^+. This is further proved by the presence of the intense K 2p peak signals for AK-MnO_2 (Figure S7A). On top of that, the drastic reconstruction process enables the formation of internal defects to a great degree, which is studied and analyzed by the depth spectra of O 1s (Figure 2D). The peaks located at 530, 531.7, and 533 eV can be finely detected, corresponding to the bonding of metal and oxygen, oxygen vacancy, and physically/chemically adsorbed O, respectively.[45,46] Impressively, the intensive peak at 531.7 eV implies a significant amount of oxygen vacancies for the as-formed AK-MnO_2 hybrids. Then, the HAADF-STEM characterization was carried out via spherical-aberration-corrected TEM to visualize the oxygen vacancies of the AK-MnO_2. As shown in Figure S8, the AK-MnO_2 displays an ultrathin and wrinkled nanosheet morphology. Notably, many created defective sites are distributed at the edge of the nanosheets (Figures 2E and S8). In addition, according to the intensity profile along the rectangular region, the missed O atom and O defect are observed. For comparison, high-crystalline MnO_2 (HC-MnO_2) was also fabricated; please refer to Figure S9 for details.

The dynamic leaching of Al is tracked by Al *K*-edge spectra, acquired via TFY and TEY scan models. As shown in Figure S6B, the Al K-edge signal in the sXAS/TEY spectrum of the Mn(Al)-OH hybrids demonstrates a decrease compared with that the MnAl-LDH and then disappears completely for the AK-MnO_2 hybrids, indicative of the gradual leaching of Al from the microstructure. Likewise, no obvious Al *K*-edge signal is demonstrated for the sXAS/TFY scan of AK-MnO_2 (Figure 2F), implying that Al has been leached completely. Furthermore, Al 2p spectra characterization was carried out, where a finely consistent result was detected (Figure S7B). To evaluate the key factors of the "nano-tailoring" process, a series of control experiments was conducted. On one hand, to understand the effect of Al, we also prepared $Mn(OH)_x$ (denoted as Mn-OH) via the same process as for the MnAl-LDH but without the addition of an Al source. It accords well with the phase structure of $Mn(OH)_2$ (Figure S4). Interestingly, when treated with the same "nano-tailoring" process as the MnAl-LDH, the Mn-OH cannot be finely and quickly reconstructed into the small nanosheets, manifesting that the deep reconstruction reaction is unfavorable or relatively poor in dynamics. For more details, please refer to Figures S10–S13. On the other hand, the effect of electrochemical CV scanning treatment is also discussed. For

Please cite this article in press as: Guo et al., *Operando* leaching of pre-incorporated Al and mechanism in transition-metal hybrids on carbon substrates for enhanced charge storage, Matter (2021), https://doi.org/10.1016/j.matt.2021.06.035

comparison, the MnAl-LDH was only immersed in 6 M KOH electrolyte, without the CV scanning treatment, and the reaction time was kept consistent with that of the "nano-tailoring" process. However, an insufficient oxidation and reconstruction process was detected (Figure S14), demonstrating that the CV scanning treatment is a vital factor to efficiently boost the structure evolution to a great degree. As mentioned above, it can be concluded that Al leaching can ensure the formation of metastable intermediates to initiate the reconstruction process, where deep oxidation and reconstruction is further facilitated and finished by the electrochemical CV scanning treatment.

To understand the underlying effects of oxygen vacancies in the microstructure of the AK-MnO_2 hybrids, DFT calculation was carried out. The AK-MnO_2 without or with oxygen vacancies was used as the model for the calculations (Figures 2G and 2I). The lattice parameters of the AK-MnO_2 used are listed in Table S1. For the AK-MnO_2 without oxygen vacancies, the total density of state (TDOS) and partial density of state (PDOS) at the Fermi level (E_F) set at 0 eV display a detectable band gap, indicative of the semiconductor properties, as illustrated in Figure 2H. With oxygen vacancies, however, continuous TDOS and PDOS (Figure 2J) near E_F can be detected, indicative of the efficient electron transfer and highly improved electrical conductivity.[47]

Moreover, the adsorption of sodium ion was decoupled. The optimized adsorption structures of hydrated sodium ion on the surface of AK-MnO_2 without or with oxygen vacancies are shown in Figures 2K and 2L. With oxygen vacancies, the hydrated sodium ion adsorption energy over the materials is −4.60 eV, which is lower than that of the AK-MnO_2 without oxygen vacancies (−4.20 eV). Thus, due to the existence of a considerable amount of oxygen vacancies, sodium ion adsorption would be energetically favorable on the surface, responsible for boosting the surface/interface reaction kinetics.

The universality of the "nano-tailoring" process and the two distinct mechanisms involved

To investigate and explore the universality of the "nano-tailoring" strategy, other extensively studied LDHs, such as CoAl-LDH and NiAl-LDH, were also prepared following a similar electrodeposition method and then treated with the "nano-tailoring" process. For the as-formed CoAl-LDH, a large nanosheet microstructure with an average size of about 325 nm can be observed (Figures 3A and 3C). Subsequently, the "nano-tailoring" process was carried out similar to that of the MnAl-LDH, triggering fast Al leaching and structure reconstruction (Figures S15 and S16). It is interesting that the derived hybrids deliver the nanosheet structure with an average size of about 50 nm with a little aggregation (Figures 3B, 3C, S16C, and S16D), displaying about seven times decrease in size compared with the pristine CoAl-LDH. The small nanosheet clusters with short electron transfer path and abundant transfer channels feature the potential to robustly boost charge-storage efficiency for fast and efficient energy storage. Moreover, as revealed by the HAADF-STEM images and the corresponding elemental maps, Co and O elements are uniformly distributed on the as-formed hybrids (Figure 3D). Similar to the AK-MnO_2, the nanosheets are also of low crystallinity (Figure 3E), due to the rapid dynamic reconstruction-induced formation of unsaturated sites and defects, thus contributing to the following high reactivity.

To gain a clearer understanding of the microstructure, the evolution of the phase components during the reconstruction process was tracked by XRD patterns in

Please cite this article in press as: Guo et al., *Operando* leaching of pre-incorporated Al and mechanism in transition-metal hybrids on carbon substrates for enhanced charge storage, Matter (2021), https://doi.org/10.1016/j.matt.2021.06.035

CellPress

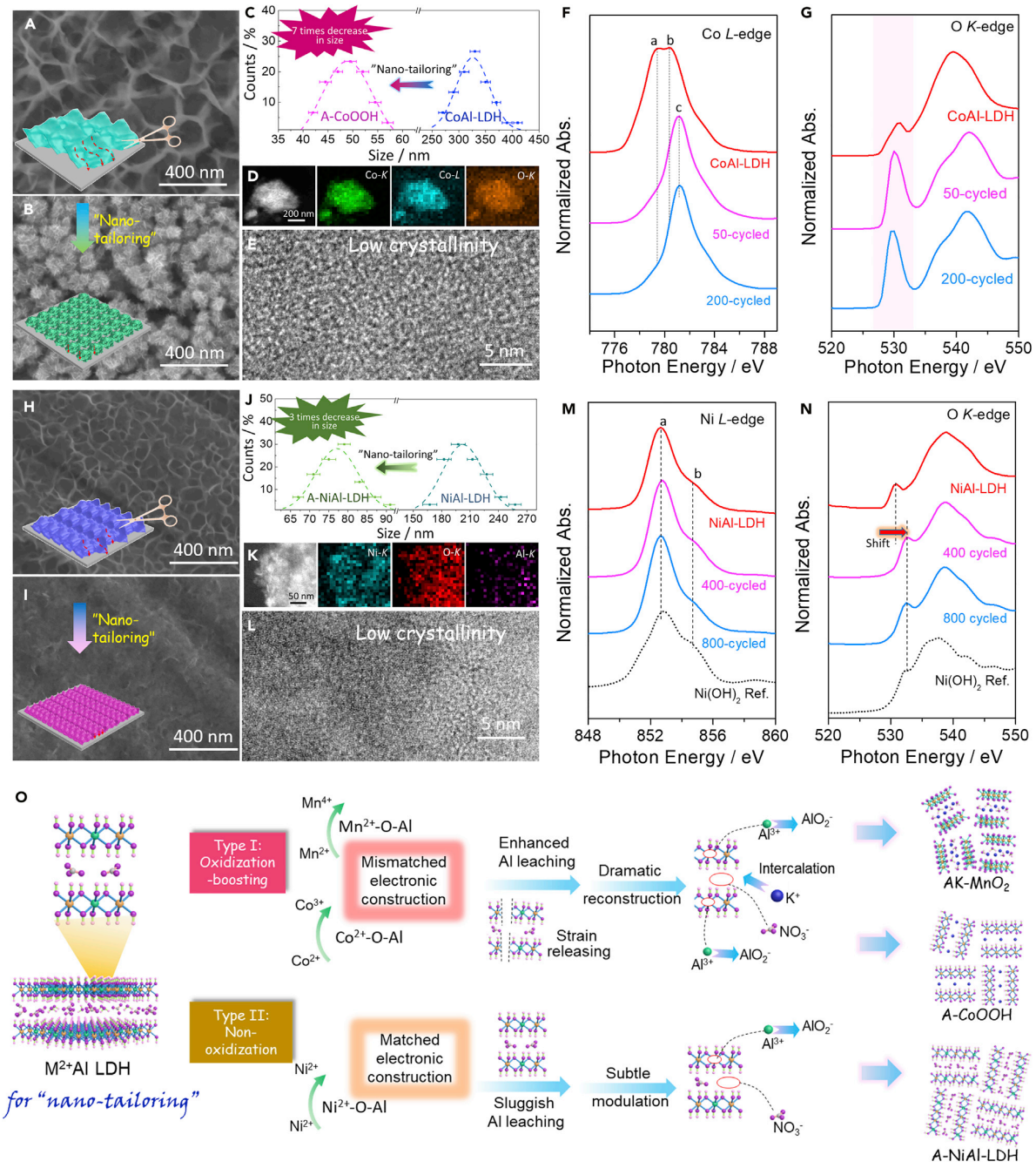

Figure 3. The application of the "nano-tailoring" strategy to configure Ni- and Co-based low-crystallinity nanosheets

(A and B) SEM images of the CoAl-LDH (A) and the 200-cycled hybrids (A-CoOOH) (B).

(C) Size distribution of the CoAl-LDH and A-CoOOH hybrids.

(D) HAADF-STEM image of the A-CoOOH and the corresponding EDS maps (*K*-edge).

(E) HR-TEM image of the A-CoOOH hybrids.

(F and G) Soft XAS spectra: Co *L*-edge (F) and O *K*-edge (G) spectra of the CoAl-LDH and the 50- and 200-cycled hybrids.

(H and I) SEM images of the NiAl-LDH (H) and the 400-cycled hybrids (A-NiAl-LDH) (I).

(J) Size distribution of the NiAl-LDH and A-NiAl-LDH hybrids.

Please cite this article in press as: Guo et al., *Operando* leaching of pre-incorporated Al and mechanism in transition-metal hybrids on carbon substrates for enhanced charge storage, Matter (2021), https://doi.org/10.1016/j.matt.2021.06.035

Figure 3. *Continued*
(K) HAADF-STEM image of the A-NiAl-LDH and the corresponding EDS maps (*K*-edge).
(L) HR-TEM image of the A-NiAl-LDH hybrids.
(M and N) Soft XAS spectra: Ni *L*-edge (M) and O *K*-edge (N) spectra of the NiAl-LDH and that after 400 and 800 cycles.
(O) Schematic illustration of the underlying principle of the "nano-tailoring" process.

detail. As the "nano-tailoring" process goes on, the CoAl-LDH is transformed to the CoOOH phase (JCPDS card no. 07-0169) with a low crystallinity after 50 electrochemical cycles (Figure S17A). After 200 cycles, the crystallinity further decreases and only the peak corresponding to the interlayer spacing can be detected, indicative of the low-crystallinity/amorphous features in the [CoO_6] laminate, thus corresponding to the HR-TEM results (Figure 3E). The final derived low-crystallinity CoOOH structure is thus labeled as A-CoOOH.

The dynamic reconstruction process was further studied by sXAS spectra. The Co *L*-edge spectrum of the CoAl-LDH displays the typical peaks a and b that can be indexed to Co^{2+}, indicative of the Co^{2+}-dominant features (Figure 3F). However, after 50 cycles, the intensity of the two peaks decreases to a great degree, while a new intensive peak emerges, denoted as peak c, that corresponds to Co^{3+}, indicative of a significant oxidization of Co^{2+} to Co^{3+}.[48] After 200 cycles (A-CoOOH), peaks a and b completely disappear, while peak c keeps a high intensity, indicative of the deep evolution and transformation from Co^{2+} to Co^{3+}. This is also confirmed by the Co 2p XPS spectra (Figure S17B), which is displayed and discussed in the supplemental information. For the O *K*-edge of the CoAl-LDH, the pre-peak at about 531.1 eV can be assigned to the hybridization of Co 3p to O 2p.[49] After 50 and 200 cycles, the peak intensity displays a significant increase, while the position demonstrates a negative shift (Figure 3G), indicative of the intensified and modulated Co-O hybridization during the evolution process. Moreover, to further understand the key role of Al, a control experiment was carried out. To be specific, $Co(OH)_2$ with a nanosheet-shaped structure was formed by a similar electrodeposition process without an Al source. Then it was treated with the same process as the CoAl-LDH. However, the nanosheets were transformed into the bulky structure instead of small nanosheets (Figure S18), vividly confirming that the *in situ* leaching of Al is of great importance for the success of the "nano-tailoring" process.

Some similar, but not exactly the same, results are witnessed for the NiAl-LDH. The NiAl-LDH fabricated through electrodeposition also displays a uniform nanosheet microstructure with an average size of about 202 nm (Figures 3H and 3J). Subsequently, the "nano-tailoring" process was allowed to proceed, and the corresponding microstructure evolution was further tracked and analyzed. Notably, the morphology displays a sluggish change, and significant structure destruction into small nanosheets (with a size of about 77 nm) is detected after 400 cycles (Figures 3I, 3J, S19A, and S19B). Moreover, as demonstrated in the HAADF-STEM image and elemental mapping images, Ni and O elements are uniformly distributed in the 400-cycled NiAl-LDH, while the signal of Al is weakened a lot compared with that of the pristine NiAl-LDH (Figures 3K and S20). And as demonstrated in the HR-TEM image (Figure 3L) and XRD results (Figure S19C), the 400-cycled NiAl-LDH also delivers low-crystallinity features like the AK-MnO_2 and A-CoOOH, and is thus denoted as A-NiAl-LDH. Somewhat surprisingly, based on the SEM/energy dispersive X-ray spectroscopy (EDS) and depth XPS results, a considerable amount of Al species was still present on the surface and subsurface after the "nano-tailoring" process (Figures S19D–S19F).

To further understand the bonding information and electronic structure, the reconstruction of the NiAl-LDH during the "nano-tailoring" process was studied and

Please cite this article in press as: Guo et al., *Operando* leaching of pre-incorporated Al and mechanism in transition-metal hybrids on carbon substrates for enhanced charge storage, Matter (2021), https://doi.org/10.1016/j.matt.2021.06.035

decoupled by sXAS spectra (TEY mode). The Ni *L*-edge spectrum of the NiAl-LDH is exactly comparable to that of the $Ni(OH)_2$ reference sample, implying that Ni^{2+} is dominant in the microstructure (Figure 3M).[50] After 400 and 800 cycles, the spectra display no appreciable changes compared with that of the pristine NiAl-LDH. With this information in mind, it can be concluded that there is no apparent increase in the valence state of Ni during the "nano-tailoring" process. Furthermore, the O *K*-edge spectra of the as-formed hybrids were also examined and analyzed (Figure 3N). The pre-peak of the O *K*-edge can be attributed to the hybridization of Ni 3d and O 2p.[51] Compared with the pristine NiAl-LDH, a positive shift of the pre-peak can be detected after 400 and 800 cycles, which becomes closer to the $Ni(OH)_2$ reference sample. This implies a tuned interaction between Ni and O during the "nano-tailoring" process, which is triggered by the irreversible Al leaching and surface electronic structure modulation.

The C *K*-edge spectra of the NiAl-LDH and that after 400 cycles (A-NiAl-LDH), as well as the CoAl-LDH and that after 200 cycles (A-CoOOH), were further examined. It is noteworthy that significant peaks at around 300 eV for A-CoOOH can be observed, corresponding to the typical peaks of K L_3-and L_2-edge, as we mentioned before. This indicates that intercalation of K^+ happens during the "nano-tailoring" process for the CoAl-LDH, which is similar to that of the MnAl-LDH. However, the typical peaks of K *L*-edge cannot be detected for the A-NiAl-LDH (Figure S21), implying that the dynamics are unfavorable or sluggish for K^+ to intercalate into the microstructure of the NiAl-LDH during the "nano-tailoring" process.

As mentioned above, some underlying principles are surely followed in the "nano-tailoring" process, which are uncovered and discussed here. In general, the reducibility of M^{2+} in LDHs acts as a vital factor in the "nano-tailoring" process, and the reconstruction mainly involves two distinct types, as illustrated in Figure 3O: (1) oxidization-boosting type (such as Mn^{2+}, Co^{2+}) and (2) non-oxidization type (such as Ni^{2+}). For the oxidization-boosting type, M^{2+} features metastable characteristics with a strong oxidation tendency. Accordingly, the as-generated strong internal strain would result in a mismatched electronic construction, thus inducing the formation of unsaturated sites and numerous defects for ultrafast Al leaching. The dramatic Al leaching results in a significant loss of positive charges, thus attracting an irreversible intercalation of the univalent charge carriers (K^+ ions) as the compensation charges.[52,53] In the meantime, K^+ may serve as an electron donor and bond with O atoms to some extent, thus weakening the bonding of M-O and producing some oxygen vacancies.[54] Finally, the phase evolution process would be accelerated. For the second type, M^{2+} is thermodynamically stable and oxidation is unfavorable, demonstrating a well-matched electronic construction and a robust interactive bonding. Due to the lack of strong internal strain effects, the phase evolution is highly restricted and sluggish in dynamics. In this case, given that Al leaching displays a slow rate, the partial removal of interlayer anions would be capable enough to maintain the charge balance well.[55] Therefore, a prodigious energy barrier would be required for K^+ intercalation, which would hardly occur. To sum up, it is exciting to note that the "nano-tailoring" process is universal for the top-down configuration of low-crystallinity and small-sized electrode materials with structural defects, although a different leaching process is presented, possessing great prospects for serving the energy and catalysis fields.

Characterization and evaluation of the electrochemical performance

The electrochemical performance of the as-made hybrids was evaluated. Impressively, for the AK-MnO_2 hybrids, even at a super-high scan rate of 1 V s^{-1}, no

Please cite this article in press as: Guo et al., *Operando* leaching of pre-incorporated Al and mechanism in transition-metal hybrids on carbon substrates for enhanced charge storage, Matter (2021), https://doi.org/10.1016/j.matt.2021.06.035

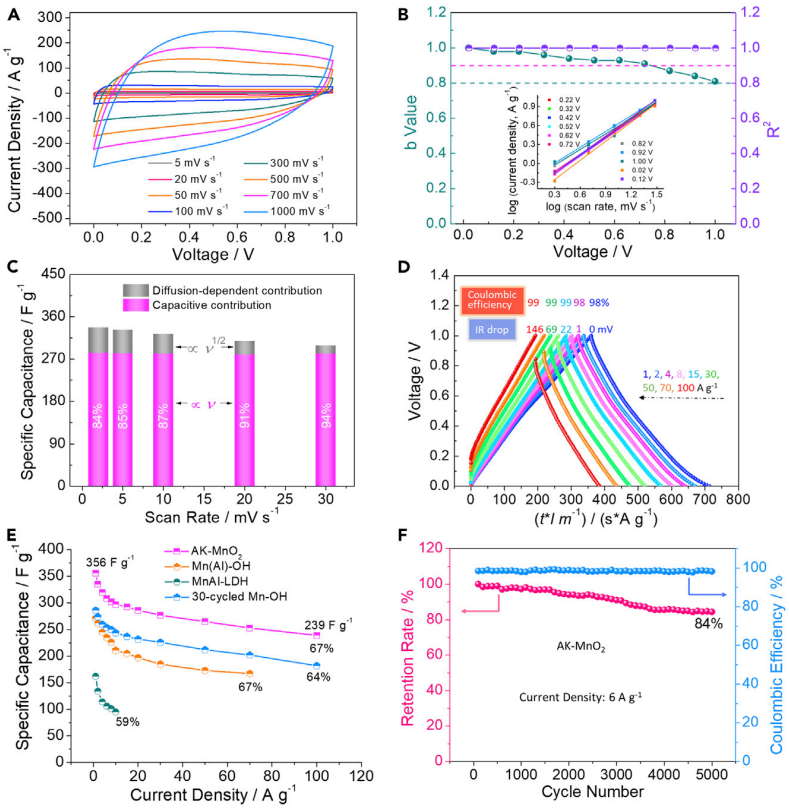

Figure 4. Electrochemical performance and comparison of the hybrids

(A) CV curves of the AK-MnO_2 hybrids at different scan rates.

(B) b values of the AK-MnO_2 at different voltages. Inset: the logarithm of current densities versus logarithm of scan rates for the AK-MnO_2 electrode.

(C) Capacitive contribution of the AK-MnO_2 at different scan rates.

(D) Galvanostatic charge/discharge curves of the AK-MnO_2.

(E) Specific capacitance of the MnAl-LDH, Mn(Al)-OH, 30-cycled Mn-OH, and AK-MnO_2 at different current densities.

(F) Cycle performance of the AK-MnO_2 hybrids at 6 A g^{-1}.

significant deformation of CV curves could be detected (Figure 4A), indicative of the superior rate performance. The charge-storage capability in terms of surface/interface reaction dynamics is further decoupled by the following equation:

$$i = av^b.$$

It can also be written as:

$$\log(i) = b\log(v) + \log(a) \text{ (a, b are constants).}$$

Here, the b value can be applied to determine surface-reaction-dominated contribution (when the b value is near 1.0) and diffusion-dominated contribution (when the b value is near 0.5). It was found that the b value for AK-MnO_2 is greater than 0.8 at different voltages, and this value is greater than 0.9 in the range of 0–0.72 V, indicative of a surface-reaction-dominated charge-storage process (Figure 4B). Subsequently, the capacitive contribution was evaluated based on the CV curves, which is explained and analyzed in Figure S22. Accordingly, it was found that the capacitive contribution

Please cite this article in press as: Guo et al., *Operando* leaching of pre-incorporated Al and mechanism in transition-metal hybrids on carbon substrates for enhanced charge storage, Matter (2021), https://doi.org/10.1016/j.matt.2021.06.035

can reach 84% at 2 mV s^{-1}, 85% at 5 mV s^{-1}, 87% at 10 mV s^{-1}, 91% at 20 mV s^{-1}, and up to 94% at 30 mV s^{-1} (Figures 4C and S22), indicative of a surface-reaction-dependent charge-storage process and responsible for a high rate performance and stability. Subsequently, electrochemical impedance spectroscopy measurements were conducted. Generally speaking, the solution resistance (R_s, obtained by the x intercept of the Nyquist plots) is used to identify the internal barrier and ion response capability, while the charge-transfer resistance (R_{ct}, obtained by the diameter of the semicircle of the Nyquist plots) is used to evaluate the charge-delivery capability at the electrode/electrolyte interface. The Nyquist plots are displayed in Figure S23. It was found that AK-MnO_2 exhibits significantly reduced R_{ct} and R_s values compared with the counterparts. And the IR drop value was 69 mV at 50 A g^{-1}, and only 146 mV even at a super-large current density of 100 A g^{-1} (Figure 4D), further indicative of a lower internal resistance. The Coulombic efficiency was 98% at 1 A g^{-1} and could reach over 98% at different current densities, manifesting the highly reversible charge-storage process, with a superior stability. Therefore, AK-MnO_2 is capable of concurrently realizing a high Coulombic efficiency and low IR drop, superior to other electrodes to some degree (Figures S24 and 25). In view of the above, the optimal mass-transport and charge-transfer kinetics can be well accomplished by engineering a highly defective, active site-enriched microstructure. The AK-MnO_2 electrode delivers a high capacitance value of 356 F g^{-1} at 1 A g^{-1}, with an ultrahigh retention rate of 67% at 100 A g^{-1}, indicative of a very sound rate performance, outperforming the Mn(Al)-OH, MnAl-LDH, HC-MnO_2, and 30-cycled Mn-OH electrodes to a great degree (Figures 4E and S25). That is to say, thanks to the "nano-tailoring" process, the microstructure is endowed with *in situ* incorporated oxygen vacancies, as well as abundant accessible area or favorable active edge sites, eventually promoting its mass-transport and charge-transfer process for efficient energy storage. In addition, a sound retention rate of 85% is realized for AK-MnO_2 after 5,000 cycles at 6 A g^{-1} (Figures 4F and S26), indicative of high stability. These decent capacitive properties are all in the front rank among previously reported MnO_2-based electrodes (Table S2). Considering the mass loss after the "nano-tailoring" process, electrodes with the same mass loading were fabricated by varying the electrodeposition time of the precursor, and their performances were further compared. As shown in Figure S27, the capacitance performance of the as-formed AK-MnO_2 is much superior to that of the counterparts. On the other hand, thanks to the "nano-tailoring" process, superior charge-storage capability can also be realized for A-CoOOH and A-NiAl-LDH; please refer to Figures S28 and S29 for details. Therefore, with the positive effects of the "nano-tailoring" process, a sharply strengthened charge-storage capability is gratifyingly reached. It is expected that these findings will provide more possibilities in the energy field and help with the generation of more insightful inspirations and attempts. Looking ahead, to enable substantial achievements in methodology, it would be highly appreciated to *operando* track the surface/interface interaction, coordination information, and spatial charge distribution. And it is highly recommended to develop time-saving, controllable, and low-cost configuration methods for upcoming green and sustainable energy systems.

Conclusion

In summary, a universal "nano-tailoring" strategy is presented here to robustly convert transition-metal hybrids into low-crystallinity, active edge sites and vacancy-enriched hybrids, where the involved phase-evolution rule is unveiled and decoupled with the help of the sXAS technique. As a representative sample, the "nano-tailoring" process triggered the transformation of the MnAl-LDH into the low-crystallinity AK-MnO_2, accompanied by the *in situ* incorporation of abundant active sites and oxygen vacancies. Furthermore, as demonstrated by the DFT calculation results,

Please cite this article in press as: Guo et al., *Operando* leaching of pre-incorporated Al and mechanism in transition-metal hybrids on carbon substrates for enhanced charge storage, Matter (2021), https://doi.org/10.1016/j.matt.2021.06.035

the oxygen vacancies in the microstructure can not only help facilitate the electron transfer process, but also boost the adsorption of hydrated Na^+ for enhanced reaction dynamics. As such, the as-formed AK-MnO_2 hybrids can deliver a high capacitance value of 356 F g^{-1} with an ultrahigh retention rate of 67% at a super-large current density of 100 A g^{-1}, indicative of a very superior rate performance. More importantly, the "nano-tailoring" process features a sound universality that can also *in situ* transform NiAl-LDH and CoAl-LDH into transition-metal hybrids with low-crystallinity and highly active microstructures. Furthermore, we propose a principle of the "nano-tailoring" process and further divide it into two main branches based on the reducibility of M^{2+} in the M^{2+}Al-LDH, (1) oxidization-boosting type and (2) non-oxidization type, where the reaction rate and structural evolution process features a substantial difference. It is expected that this "nano-tailoring" strategy will provide and spur many opportunities and ideas for configuring kinetically favorable nanomaterials, serving as a good model and reference for the development of materials adopted in the energy- and catalysis-related fields.

EXPERIMENTAL PROCEDURES

Resource availability

Lead contact

Further information and requests for resources and reagents should be directed to and will be fulfilled by the lead contact, Jieshan Qiu (jqiu@dlut.edu.cn, qiujs@mail.buct.edu.cn).

Materials availability

All chemicals were purchased from commercial suppliers and used directly without further purification: $Mn(NO_3)_2$ aqueous solution, $Al(NO_3)_3{\cdot}9H_2O$, and $Ni(NO_3)_2{\cdot}6H_2O$ were purchased from Xilong Scientific Co., Ltd.; $Co(NO_3)_2{\cdot}6H_2O$, $KMnO_4$, KOH, and Na_2SO_4 were purchased from Tianjin Kemiou Chemical Reagent Co., Ltd.; and the carbon fiber was purchased from Shanghai Hesen Electric Co., Ltd.

Data and code availability

This study did not generate/analyze datasets/code.

Fabrication of the MnAl-LDH, Mn(Al)-OH, and AK-MnO_2

The MnAl-LDH nanosheets were fabricated by a simple electrodeposition method. First, CP (2 × 3.3 cm^2) was treated in 80 mL of concentrated nitric acid for 24 h to form a hydrophilic surface. After that, 0.6 mmol $Mn(NO_3)_2$ and 0.4 mmol $Al(NO_3)_3$ were dissolved in 50 mL of deionized water under continuous stirring for 5 min, forming a light pink, transparent solution for electrodeposition. Then pre-treated CP, saturated calomel electrode, and Pt plate (2 × 2 cm^2) were used as working electrode, reference electrode, and counter electrode, respectively. The electrodeposition process was carried out on a CHI760D electrochemical workstation at a voltage of −1.5 V for 10 min, yielding the MnAl-LDH on CP. Next, the as-formed MnAl-LDH hybrids were soaked in 6 M KOH electrolyte for 2 min, yielding the Mn(Al)-OH. Then, it was further cycled by a CV technique with a voltage range of 0–0.6 V for 30 cycles, yielding the AK-MnO_2 hybrids.

Fabrication of the Mn-OH

In comparison, the Mn-OH hybrids were formed by a similar electrodeposition process without the addition of an Al source. The as-formed hybrids were washed with water and ethanol thoroughly and dried at 60°C for 2 h.

Fabrication of the HC-MnO_2

For the fabrication of the HC-MnO_2, pre-treated CP (2 × 3.3 cm^2) was immersed into 40 mL aqueous solution containing 0.316 g $KMnO_4$. After being treated at 180°C for 3 h in a Teflon-lined autoclave, the HC-MnO_2 was formed. It was washed with water and ethanol thoroughly and dried at 60°C for 2 h.

Computational methods

The calculations, based on DFT, were carried out by the CASTEP module in Materials Studio[56] (version 8.0, Accerly Corporation). The electron-ion interaction was described by Vanderbilt-type ultrasoft pseudopotentials and the exchange-correlation function was treated using the generalized gradient approximation (GGA) of Perdew et al. as parameterized by Perdew-Burk-Ernzerhof and with spin-polarized consideration.[57,58] For the present study, the GGA + U calculation with an empirical Coulomb repulsion term U value of 3.9 eV was employed for the d-like states of Mn atoms.[59] The energy cut-off of 520 eV was set for the plane-wave basis set and a 3 × 8×3 net was used with the Brillouin zone sampling scheme of a Monkhorst-Pack grid.[60] For highly precise results, self-consistent field tolerance was 1.0 × 10^{-6} eV/atom.

First, the geometrical optimization was performed and the convergence was defined as an ultrafine tolerance with 5 × 10^{-6} eV $atom^{-1}$ of the difference in total energy, 0.01 eV $Å^{-1}$ of maximum force, 0.02 GPa of maximum stress, and 5 × 10^{-4} Å maximum atomic displacement. After the optimization of the unit cells, the calculations of single-point energy were performed and the TDOS and PDOS of AK-MnO_2 with and without oxygen vacancies were obtained.

For the calculations of adsorption energy, since the (001) facet is exposed naturally and is more stable with lower surface energy than the dominant (110) facet,[47] the (001) facet was cleaved and slab models with a 15 Å vacuum gap that were perpendicular to the surface were built. The Brillouin zone sampling was restricted to 3 × 4 × 1 k-points due to the larger size of the unit cell. After geometrical optimization of the slab, hydrated sodium ion was added to the surface and the subsequent optimizations and calculations of single-point energy were performed with fixed size of the unit cell, because the introduction of ion did not significantly change the size and shape of the cell. The hydrated sodium ion was optimized in a 15 × 15 × 15 $Å^3$ cubic box with the Γ-point and the same stopping criterion.

The adsorption energy (E_{ads}) of the hydrated sodium ion on the surface was computed from three pairs given by:

$$E_{ads} = E_{(H2O/Na^+\text{-}KMnO2)} - (E_{KMnO2} + E_{H2O/Na^+}),$$

where $E_{H2O/Na^+\text{-}KMnO2}$ is the total energy of the hydrated sodium ion adsorbed onto the (001) surface at the hollow site, E_{KMnO2} is the energy of the AK-MnO_2 slab, and E_{H2O/Na^+} is the energy of the hydrated sodium ion.

SUPPLEMENTAL INFORMATION

Supplemental information can be found online at https://doi.org/10.1016/j.matt.2021.06.035.

ACKNOWLEDGMENTS

This work was partly supported by the National Natural Science Foundation of China (nos. 51872035, U1508201, 51673156). W.G. appreciates the great support from the Chinese Scholarship Council (no. 201906060084). This research used resources of

the Advanced Light Source, a DOE Office of Science User facility under contract DE-AC02-05CH11231. K.Q. and M.T. acknowledge support from the NSF (CHE-1665284).

AUTHOR CONTRIBUTIONS

C.Y., Q.Z., J.G., and J.Q. supervised the study. W.G. and C.Y. designed the research. W.G. carried out materials fabrication and most of the characterization. C.Y., Q.Z., J.G., and J.Q. provided constructive advice for experiments. W.G., F.Y., Y.L., Y.Z., and X.F. carried out the soft X-ray measurements. J.C., K.Q., and M.T. carried out DFT calculations. W.G., Y.X., J. Yu, and K.L. performed electrochemical measurements. J. Yang, S.L., and Z.W. performed the TEM measurements. All authors discussed the results and commented on the manuscript.

DECLARATION OF INTERESTS

The authors declare no competing interests.

Received: March 9, 2021
Revised: May 18, 2021
Accepted: June 17, 2021
Published: July 15, 2021

REFERENCES

1. Simon, P., and Gogotsi, Y. (2020). Perspectives for electrochemical capacitors and related devices. Nat. Mater. *19*, 1151–1163.
2. Noori, A., El-Kady, M.F., Rahmanifar, M.S., Kaner, R.B., and Mousavi, M.F. (2019). Towards establishing standard performance metrics for batteries, supercapacitors and beyond. Chem. Soc. Rev. *48*, 1272–1341.
3. Salanne, M., Rotenberg, B., Naoi, K., Kaneko, K., Taberna, P.L., Grey, C.P., Dunn, B., and Simon, P. (2016). Efficient storage mechanisms for building better supercapacitors. Nat. Energy *1*, 16070.
4. Nakhanivej, P., Yu, X., Park, S.K., Kim, S., Hong, J.Y., Kim, H.J., Lee, W., Hwang, J.Y., Yang, J.E., Wolverton, C., et al. (2019). Revealing molecular-level surface redox sites of controllably oxidized black phosphorus nanosheets. Nat. Mater. *18*, 156–162.
5. Guo, W., Yu, C., Li, S.F., and Qiu, J.S. (2021). Toward commercial-level mass-loading electrodes for supercapacitors: opportunities, challenges and perspectives. Energy Environ. Sci. *14*, 576–601.
6. Xia, Y., Mathis, T.S., Zhao, M.Q., Anasori, B., Dang, A., Zhou, Z., Cho, H., Gogotsi, Y., and Yang, S. (2018). Thickness-independent capacitance of vertically aligned liquid-crystalline MXenes. Nature *557*, 409–412.
7. Guo, W., Yu, C., Li, S.F., Wang, Z., Yu, J.H., Huang, H.W., and Qiu, J.S. (2019). Strategies and insights towards the intrinsic capacitive properties of MnO_2 for supercapacitors: challenges and perspectives. Nano Energy *57*, 459–472.
8. Choi, C., Ashby, D.S., Butts, D.M., DeBlock, R.H., Wei, Q., Lau, J., and Dunn, B. (2020). Achieving high energy density and high power density with pseudocapacitive materials. Nat. Rev. Mater. *5*, 5–19.
9. Tan, C., Cao, X., Wu, X.J., He, Q., Yang, J., Zhang, X., Chen, J., Zhao, W., Han, S., Nam, G.H., et al. (2017). Recent advances in ultrathin two-dimensional nanomaterials. Chem. Rev. *117*, 6225–6331.
10. Sun, Z.P., Martinez, A., and Wang, F. (2016). Optical modulators with 2D layered materials. Nat. Photon. *10*, 227–238.
11. Guo, W., Yu, C., Li, S.F., Song, X.D., Yang, Y., Qiu, B., Zhao, C.T., Huang, H.W., Yang, J., Han, X.T., et al. (2019). A phase transformation-resistant electrode enabled by a MnO_2-confined effect for enhanced energy storage. Adv. Funct. Mater. *29*, 1901342.
12. El-Kady, M.F., Ihns, M., Li, M.P., Hwang, J.Y., Mousavi, M.F., Chaney, L., Lech, A.T., and Kaner, R.B. (2015). Engineering three-dimensional hybrid supercapacitors and microsupercapacitors for high-performance integrated energy storage. Proc. Natl. Acad. Sci. U S A *112*, 4233–4238.
13. Hu, Y.T., Wu, Y., and Wang, J. (2018). Manganese-oxide-based electrode materials for energy storage applications: how close are we to the theoretical capacitance? Adv. Mater. *30*, 1802569.
14. Guo, W., Yu, C., Li, S.F., Yang, J., Liu, Z.B., Zhao, C.T., Huang, H.W., Zhang, M.D., Han, X.T., Niu, Y.Y., et al. (2017). High-stacking-density, superior-roughness LDH bridged with vertically aligned graphene for high-performance asymmetric supercapacitors. Small *13*, 1701288.
15. Liu, J.Q., Zheng, M.B., Shi, X.Q., Zeng, H.B., and Xia, H. (2016). Amorphous FeOOH quantum dots assembled mesoporous film anchored on graphene nanosheets with superior electrochemical performance for supercapacitors. Adv. Funct. Mater. *26*, 919–930.
16. Li, Q., Xu, Y., Zheng, S., Guo, X., Xue, H., and Pang, H. (2018). Recent progress in some amorphous materials for supercapacitors. Small *14*, 1800426.
17. Shi, P.P., Li, L., Hua, L., Qian, Q.Q., Wang, P.F., Zhou, J.Y., Sun, G.Z., and Huang, W. (2017). Design of amorphous manganese oxide@multiwalled carbon nanotube fiber for robust solid-state supercapacitor. ACS Nano *11*, 444–452.
18. Zhao, Y., Zheng, L., Shi, R., Zhang, S., Bian, X., Wu, F., Cao, X., Waterhouse, G.I.N., and Zhang, T. (2020). Alkali etching of layered double hydroxide nanosheets for enhanced photocatalytic N_2 reduction to NH_3. Adv. Energy Mater. *10*, 2002199.
19. Zhao, Y., Zhao, Y., Shi, R., Wang, B., Waterhouse, G.I.N., Wu, L.Z., Tung, C.H., and Zhang, T. (2019). Tuning oxygen vacancies in ultrathin TiO_2 nanosheets to boost photocatalytic nitrogen fixation up to 700 nm. Adv. Mater. *31*, 1806482.
20. Li, C., Wang, T., Zhao, Z.J., Yang, W., Li, J.F., Li, A., Yang, Z., Ozin, G.A., and Gong, J. (2018). Promoted fixation of molecular nitrogen with surface oxygen vacancies on plasmon-enhanced TiO_2 photoelectrodes. Angew. Chem. Int. Ed. *57*, 5278–5282.
21. Yan, D., Li, Y., Huo, J., Chen, R., Dai, L., and Wang, S. (2017). Defect chemistry of nonprecious-metal electrocatalysts for oxygen reactions. Adv. Mater. *29*, 1606459.
22. Bai, S., Zhang, N., Gao, C., and Xiong, Y. (2018). Defect engineering in photocatalytic materials. Nano Energy *53*, 296–336.

Please cite this article in press as: Guo et al., *Operando* leaching of pre-incorporated Al and mechanism in transition-metal hybrids on carbon substrates for enhanced charge storage, Matter (2021), https://doi.org/10.1016/j.matt.2021.06.035

23. Shi, R., Zhao, Y., Waterhouse, G.I.N., Zhang, S., and Zhang, T. (2019). Defect engineering in photocatalytic nitrogen fixation. ACS Catal. *9*, 9739–9750.

24. Wang, L., Zhang, Y., Chen, L., Xu, H., and Xiong, Y. (2018). 2D polymers as emerging materials for photocatalytic overall water splitting. Adv. Mater. *30*, 1801955.

25. Chen, J., Han, Y., Kong, X., Deng, X., Park, H.J., Guo, Y., Jin, S., Qi, Z., Lee, Z., Qiao, Z., et al. (2016). The origin of improved electrical double-layer capacitance by inclusion of topological defects and dopants in graphene for supercapacitors. Angew. Chem. Int. Ed. *55*, 13822–13827.

26. Li, H.B., Yu, M.H., Wang, F.X., Liu, P., Liang, Y., Xiao, J., Wang, C.X., Tong, Y.X., and Yang, G.W. (2013). Amorphous nickel hydroxide nanospheres with ultrahigh capacitance and energy density as electrochemical pseudocapacitor materials. Nat. Commun. *4*, 1894.

27. Owusu, K.A., Qu, L.B., Li, J.T., Wang, Z.Y., Zhao, K.N., Yang, C., Hercule, K.M., Lin, C., Shi, C.W., Wei, Q.L., et al. (2017). Low-crystalline iron oxide hydroxide nanoparticle anode for high-performance supercapacitors. Nat. Commun. *8*, 14264.

28. Yang, J., Yu, C., Fan, X.M., Liang, S.X., Li, S.F., Huang, H.W., Ling, Z., Hao, C., and Qiu, J.S. (2016). Electroactive edge site-enriched nickel-cobalt sulfide into graphene frameworks for high-performance asymmetric supercapacitors. Energy Environ. Sci. *9*, 1299–1307.

29. Guo, W., Yu, C., Zhao, C.T., Wang, Z., Li, S.F., Yu, J.H., Tan, X.Y., Xie, Y.Y., Yang, L., Huang, H.L., et al. (2020). Boosting charge storage in 1D manganese oxide-carbon composite by phosphorus-assisted structural modification for supercapacitor applications. Energy Storage Mater. *31*, 172–180.

30. Yang, P.Y., Wu, Z.Y., Jiang, Y.C., Pan, Z.C., Tian, W.C., Jiang, L., and Hu, L.F. (2018). Fractal $(Ni_xCo_{1-x})_9Se_8$ nanodendrite arrays with highly exposed surface for wearable, all-solid-state supercapacitor. Adv. Energy Mater. *8*, 1801392.

31. Guo, W., Yu, C., Li, S.F., Song, X.D., Huang, H.W., Han, X.T., Wang, Z., Liu, Z.B., Yu, J.H., Tan, X.Y., et al. (2019). A universal converse voltage process for triggering transition metal hybrids in situ phase restruction toward ultrahigh-rate supercapacitors. Adv. Mater. *31*, 1901241.

32. Yan, Z., Sun, H., Chen, X., Liu, H., Zhao, Y., Li, H., Xie, W., Cheng, F., and Chen, J. (2018). Anion insertion enhanced electrodeposition of robust metal hydroxide/oxide electrodes for oxygen evolution. Nat. Commun. *9*, 2373.

33. Lim, J., Maiti, U.N., Kim, N.Y., Narayan, R., Lee, W.J., Choi, D.S., Oh, Y., Lee, J.M., Lee, G.Y., Kang, S.H., et al. (2016). Dopant-specific unzipping of carbon nanotubes for intact crystalline graphene nanostructures. Nat. Commun. *7*, 10364.

34. Huang, H.W., Yu, C., Huang, H.L., Zhao, C.T., Qiu, B., Yao, X.C., Li, S.F., Han, X.T., Guo, W., Dai, L.M., et al. (2019). Activation of transition metal oxides by in-situ electro-regulated structure-reconstruction for ultra-efficient oxygen evolution. Nano Energy *58*, 778–785.

35. Niu, S., Jiang, W.J., Wei, Z., Tang, T., Ma, J., Hu, J.S., and Wan, L.J. (2019). Se-doping activates FeOOH for cost-effective and efficient electrochemical water oxidation. J. Am. Chem. Soc. *141*, 7005–7013.

36. Lin, B., Zhu, X., Fang, L., Liu, X., Li, S., Zhai, T., Xue, L., Guo, Q., Xu, J., and Xia, H. (2019). Birnessite nanosheet arrays with high K content as a high-capacity and ultrastable cathode for K-ion batteries. Adv. Mater. *31*, 1900060.

37. Dong, Z.H., Lin, F., Yao, Y.H., and Jiao, L.F. (2019). Crystalline $Ni(OH)_2$/amorphous $NiMoO_x$ mixed-catalyst with Pt-like performance for hydrogen production. Adv. Energy Mater. *9*, 1902703.

38. Julien, C. (2003). Raman spectra of birnessite manganese dioxides. Solid State Ionics *159*, 345–356.

39. Yang, W., and Devereaux, T.P. (2018). Anionic and cationic redox and interfaces in batteries: advances from soft X-ray absorption spectroscopy to resonant inelastic scattering. J. Power Sources *389*, 188–197.

40. Lin, F., Nordlund, D., Markus, I.M., Weng, T.-C., Xin, H.L., and Doeff, M.M. (2014). Profiling the nanoscale gradient in stoichiometric layered cathode particles for lithium-ion batteries. Energy Environ. Sci. *7*, 3077–3085.

41. Kuppan, S., Shukla, A.K., Membreno, D., Nordlund, D., and Chen, G. (2017). Revealing anisotropic spinel formation on pristine Li- and Mn-rich layered oxide surface and its impact on cathode performance. Adv. Energy Mater. *7*, 1602010.

42. Henderson, C.M.B., Cressey, G., and Redfern, S.A.T. (1995). Geological applications of synchrotron radiation. Radiat. Phys. Chem. *45*, 459–481.

43. Oishi, M., Yamanaka, K., Watanabe, I., Shimoda, K., Matsunaga, T., Arai, H., Ukyo, Y., Uchimoto, Y., Ogumi, Z., and Ohta, T. (2016). Direct observation of reversible oxygen anion redox reaction in Li-rich manganese oxide, Li_2MnO_3, studied by soft X-ray absorption spectroscopy. J. Mater. Chem. A *4*, 9293–9302.

44. Dey, A., Krishnamurthy, S., Bowen, J., Nordlund, D., Meyyappan, M., and Gandhiraman, R.P. (2018). Plasma jet printing and in situ reduction of highly acidic graphene oxide. ACS Nano *12*, 5473–5481.

45. Bao, J., Zhang, X.D., Fan, B., Zhang, J.J., Zhou, M., Yang, W.L., Hu, X., Wang, H., Pan, B.C., and Xie, Y. (2015). Ultrathin spinel-structured nanosheets rich in oxygen deficiencies for enhanced electrocatalytic water oxidation. Angew. Chem. Int. Ed. *54*, 7399–7404.

46. Fang, G.Z., Zhu, C.Y., Chen, M.H., Zhou, J., Tang, B.Y., Cao, X.X., Zheng, X.S., Pan, A.Q., and Liang, S.Q. (2019). Suppressing manganese dissolution in potassium manganate with rich oxygen defects engaged high-energy-density and durable aqueous zinc-ion battery. Adv. Funct. Mater. *29*, 1808375.

47. Zhao, Y.X., Chang, C., Teng, F., Zhao, Y.F., Chen, G.B., Shi, R., Waterhouse, G.I.N., Huang, W.F., and Zhang, T.R. (2017). Defect-engineered ultrathin δ-MnO_2 nanosheet arrays as bifunctional electrodes for efficient overall water splitting. Adv. Energy Mater. *7*, 1700005.

48. Long, X., Yu, P., Zhang, N., Li, C., Feng, X., Ren, G., Zheng, S., Fu, J., Cheng, F., and Liu, X. (2019). Direct spectroscopy for probing the critical role of partial covalency in oxygen reduction reaction for cobalt-manganese spinel oxides. Nanomaterials *9*, 577.

49. Zhou, S.M., Miao, X.B., Zhao, X., Ma, C., Qiu, Y.H., Hu, Z.P., Zhao, J.Y., Shi, L., and Zeng, J. (2016). Engineering electrocatalytic activity in nanosized perovskite cobaltite through surface spin-state transition. Nat. Commun. *7*, 11510.

50. Zheng, X.L., Zhang, B., De Luna, P., Liang, Y.F., Comin, R., Voznyy, O., Han, L., García de Arquer, F.P., Liu, M., Dinh, C.T., et al. (2018). Theory-driven design of high-valence metal sites for water oxidation confirmed using in situ soft X-ray absorption. Nat. Chem. *10*, 149–154.

51. Lin, F., Nordlund, D., Weng, T.-C., Zhu, Y., Ban, C., Richards, R.M., and Xin, H.L. (2014). Phase evolution for conversion reaction electrodes in lithium-ion batteries. Nat. Commun. *5*, 3358.

52. Zhu, X.H., Meng, F.Q., Zhang, Q.H., Xue, L., Zhu, H., Lan, S., Liu, Q., Zhao, J., Zhuang, Y.H., Guo, Q.B., et al. (2020). $LiMnO_2$ cathode stabilized by interfacial orbital ordering for sustainable lithium-ion batteries. Nat. Sustain. https://doi.org/10.1038/s41893-41020-00660-41899.

53. Xia, Q., Zhang, Q., Sun, S., Hussain, F., Zhang, C., Zhu, X., Meng, F., Liu, K., Geng, H., Xu, J., et al. (2020). Tunnel intergrowth Li_xMnO_2 nanosheet arrays as 3D cathode for high-performance all-solid-state thin film lithium microbatteries. Adv. Mater. *33*, 2003524.

54. Xu, W.J., Lyu, F.L., Bai, Y.C., Gao, A.Q., Feng, J., Cai, Z.X., and Yin, Y.D. (2018). Porous cobalt oxide nanoplates enriched with oxygen vacancies for oxygen evolution reaction. Nano Energy *43*, 110–116.

55. Wang, Y., Zhu, Y.L., Zhao, S.L., She, S.X., Zhang, F.F., Chen, Y., Williams, T., Gengenbach, T., Zu, L.H., Mao, H.Y., et al. (2020). Anion etching for accessing rapid and deep self-reconstruction of precatalysts for water oxidation. Matter *3*, 2124–2137.

56. Clark, S.J., Segall, M.D., Pickard, C.J., Hasnip, P.J., Probert, M.I.J., Refson, K., and Payne, M.C. (2005). First principles methods using CASTEP. Z. Kristallogr. Cryst. Mater. *220*, 567–570.

57. Vanderbilt, D. (1990). Soft self-consistent pseudopotentials in a generalized eigenvalue formalism. Phys. Rev. B *41*, 7892–7895.

58. Perdew, J.P., Burke, K., and Ernzerhof, M. (1996). Generalized gradient approximation made simple. Phys. Rev. Lett. *77*, 3865–3868.

59. Dudarev, S.L., Botton, G.A., Savrasov, S.Y., Humphreys, C.J., and Sutton, A.P. (1998). Electron-energy-loss spectra and the structural stability of nickel oxide: an LSDA+U study. Phys. Rev. B *57*, 1505–1509.

60. Monkhorst, H.J., and Pack, J.D. (1976). Special points for Brillouin-zone integrations. Phys. Rev. B *13*, 5188–5192.